

Chip-scale generation of 60-mode continuous-variable cluster states

Ze Wang,^{1,*} Kangkang Li,^{1,*†} Yue Wang,^{1,*} Xin Zhou,² Yinke Cheng,^{1,2} Boxuan Jing,¹ Fengxiao Sun,¹,
Jincheng Li,² Zhilin Li,² Qihuang Gong,^{1,3,4} Qiongyi He,^{1,3,4†} Bei-Bei Li,^{2,†} and Qi-Fan Yang^{1,3,4†}

¹State Key Laboratory for Artificial Microstructure and Mesoscopic Physics and Frontiers Science
Center for Nano-optoelectronics, School of Physics, Peking University, Beijing, 100871, China

²Beijing National Laboratory for Condensed Matter Physics, Institute
of Physics, Chinese Academy of Sciences, Beijing, 100190, China

³Collaborative Innovation Center of Extreme Optics, Shanxi University, Taiyuan, 030006, China

⁴Peking University Yangtze Delta Institute of Optoelectronics, Nantong, Jiangsu, 226010, China

*These authors contributed equally to this work.

†Corresponding author: kangkangli@pku.edu.cn;

qiongyihe@pku.edu.cn; libeiBei@iphy.ac.cn; leonardoyoung@pku.edu.cn.

Increasing the number of entangled entities is crucial for achieving exponential computational speedups¹ and secure quantum networks^{2,3}. Despite recent progress in generating large-scale entanglement through continuous-variable (CV) cluster states⁴⁻⁷, translating these technologies to photonic chips has been hindered by decoherence, limiting the number of entangled entities to 8⁸. Here, we demonstrate 60-mode CV cluster states in a chip-based optical microresonator pumped by chromatic lasers. Resonantly-enhanced four-wave mixing processes establish entanglement between equidistant spectral quantum modes (qumodes), forming a quantum analogue of optical frequency combs. Decoherence is minimized to achieve unprecedented two-mode raw squeezing (>3 dB) from a chip. Using bichromatic and trichromatic pump lasers, we realize one- and two-dimensional cluster states with up to 60 qumodes. Our work provides a compact and scalable platform for constructing large-scale entangled quantum resources, which are appealing for performing computational and communicational tasks with quantum advantages^{9,10}.

Quantum entanglement¹¹, as conceptualized by Einstein, Podolsky, Rosen (EPR)¹², and Schrödinger¹³, has spurred numerous quantum technologies that promise superior speed and security over classical counterparts. The key to these applications is the number of entangled entities, and if they are entangled in certain graph structures to form cluster states, novel quantum protocols such as measurement-based quantum computing¹⁴⁻¹⁹ and unconditional quantum teleportation²⁰ can be implemented. Optical photons provide appealing versatility for performing quantum computational tasks and transmitting quantum information over long distances. However, the probabilistic nature of photon sources has delayed the construction of large-scale cluster states, achieving a maximum size of 12 photons²¹ or 18 photonic qubits²².

Instead of qubits, EPR's original concept of quantum entanglement was encoded in continuous variables

(CVs), such as the positions and momenta of particles¹². This form of quantum entity, known as quantum modes (qumodes), can be deterministically entangled via Gaussian operations^{23,24}. In quantum optics, these CVs are typically represented as quadrature components, defined as $\hat{x} = (\hat{a} + \hat{a}^\dagger)/\sqrt{2}$ and $\hat{p} = -i(\hat{a} - \hat{a}^\dagger)/\sqrt{2}$, with \hat{a} (\hat{a}^\dagger) being the annihilation (creation) operator of the quantized electromagnetic field. The generation of photonic CV cluster states begins with squeezed vacuums provided by optical parametric amplifiers or oscillators, which can be multiplexed across spectral^{5,25-28}, temporal^{4,6,7,10,29-32}, path^{8,33}, and spatial^{34,35} domains. Notably, CV cluster states generated in spectral and temporal domains have achieved remarkable scales, reaching up to 60 spectral⁵ or one million temporal³² qumodes.

Efforts to translate quantum technologies onto photonic chips^{36,37} have recently focused on generating squeezed light using waveguide parametric amplifiers³⁸⁻⁴² and nonlinear optical microresonators⁴³⁻⁵³. The key performance metric, raw squeezing, measures the reduced quadrature noise relative to the vacuum noise as received by photodetectors and is critical for implementing advanced quantum algorithms^{16,19,54} and leveraging the measurement precision⁵⁵⁻⁵⁷. However, current on-chip squeezers have not matched this performance of table-top instruments⁵⁸ due to decoherence. This limitation has also restricted the scale of chip-based CV cluster states, currently capped at 8 qumodes⁸. In this work, we improve the raw squeezing of microresonator-based optical parametric oscillators to a record-high level of 3 dB. By pumping the microresonator with chromatic lasers, we deterministically entangle 60 spectral qumodes through Kerr-induced four-wave mixing (FWM) processes. The cluster state structures can be tailored to one or two dimensions by programming the pump lasers.

Results

Principle

Our protocol to generate CV cluster states belongs to the category of quantum frequency combs⁵⁹. As shown in Fig. 1, the microresonator hosts a series of longitu-

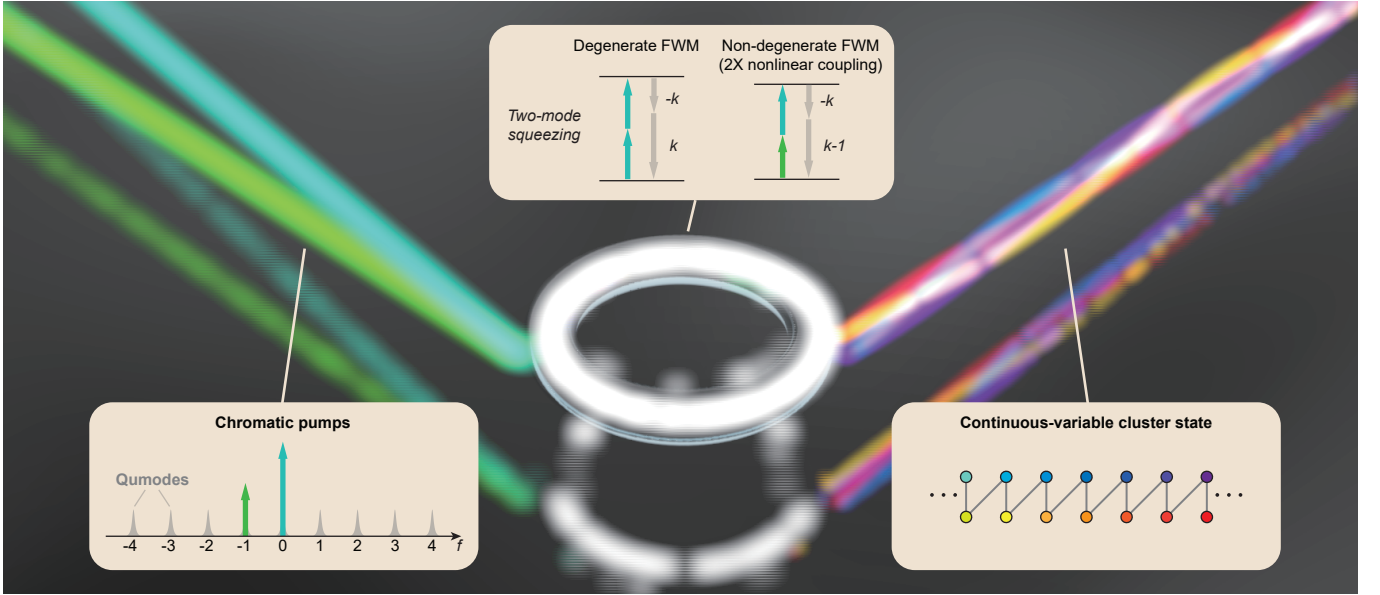


Fig. 1. Schematic illustration of continuous-variable (CV) cluster states generated in a microresonator. The microresonator hosts many spectral qumodes, and several qumodes are simultaneously pumped by continuous-wave lasers. Two-mode squeezing is induced by the four-wave mixing (FWM) processes in the microresonator. The qumodes are entangled into a CV cluster state and emitted from the microresonator for detection.

dinal modes separated by the free spectral range (FSR). Equally spaced chromatic pump lasers are coupled to the microresonator, with their spacing (f_r) closely matched to the FSR to ensure resonant excitation. The qumodes are equidistantly defined in the spectral domain with the same spacing f_r , forming a quantum analogue of optical frequency combs⁶⁰. Table-top demonstrations of quantum frequency combs typically rely on second-order nonlinear interactions^{5,25–28}. Microresonators, however, offer sufficiently high quality (Q) factors and small mode volumes that enable parametric oscillations based on Kerr nonlinearity⁶¹, which has led to both classical^{62,63} and quantum^{49,51,64} microcombs. We exploit Kerr nonlinearity to induce squeezing between the qumodes. Consider bichromatic pumps excited at modes -1 and 0, with qumodes indexed relative to the pump lasers. Multiple FWM processes occur within the microresonator, and the Hamiltonian directly describing the two-mode squeezing operations is:

$$\hat{H}_{\text{int}} = - \sum_{k>0} (gA_0A_0\hat{a}_k^\dagger\hat{a}_{-k}^\dagger + gA_{-1}A_{-1}\hat{a}_k^\dagger\hat{a}_{-k-2}^\dagger + 2gA_0A_{-1}\hat{a}_k^\dagger\hat{a}_{-k-1}^\dagger) + \text{h.c.} \quad (1)$$

Here, A_0 and A_{-1} represent the classical coherent pumps, and g is the nonlinear coupling coefficient. The annihilation (creation) operator of the k_{th} qumode is denoted by a_k (a_k^\dagger). The additional factor of 2 in the third term arises from the non-degenerate FWM process. If the power of the two pumps is set equal, this term becomes dominant, and squeezing is predominantly observed in qumode pairs with indices summing to -1. To balance

these nonlinear processes, the pump power at mode -1 can be adjusted to approximately one-quarter of the power at mode 0. This ensures $|gA_0A_0| \approx |2gA_0A_{-1}|$, providing two squeezing operations with similar efficacy. Consequently, each qumode is entangled with two others, forming a chain-like cluster state. Adjusting the pump power levels to equalize the FWM processes can be extended to devise pump lasers with more colors, leading to cluster states with distinct graph structures.

Experimental setup

The experimental setup, illustrated in Fig. 2a, utilizes an electro-optic (EO) comb synthesized from a continuous-wave laser via sequential phase and amplitude modulation⁶⁵. The EO comb generates over 70 comb lines with nearly uniform intensities (Extended Data Fig. 1). A programmable multi-port waveshaper selectively picks specific comb lines from the EO comb, allowing individual control over their phases and amplitudes. One port provides the chromatic pump lasers directed into the microresonator, while the second port functions as a local oscillator (LO), combined with the microresonator emission through a 50/50 beam splitter. These mixed signals are directed into free space, dispersed by a grating, and spatially filtered to remove residual pump lasers. The filtered signals are recombined using a matching grating for balanced homodyne detection, yielding electrical signals expressed as $\sum_k e^{-i\psi} E_k \hat{a}_k + \text{h.c.}$, where E_k represents the classical coherent fields on the k_{th} mode of the LO and ψ the relative phases between the two arms. This signal can be decomposed as a linear combination of the quadrature operators of the qumodes, \hat{x}_k and \hat{p}_k , and the noise acquired by an electrical spectral analyzer (ESA)

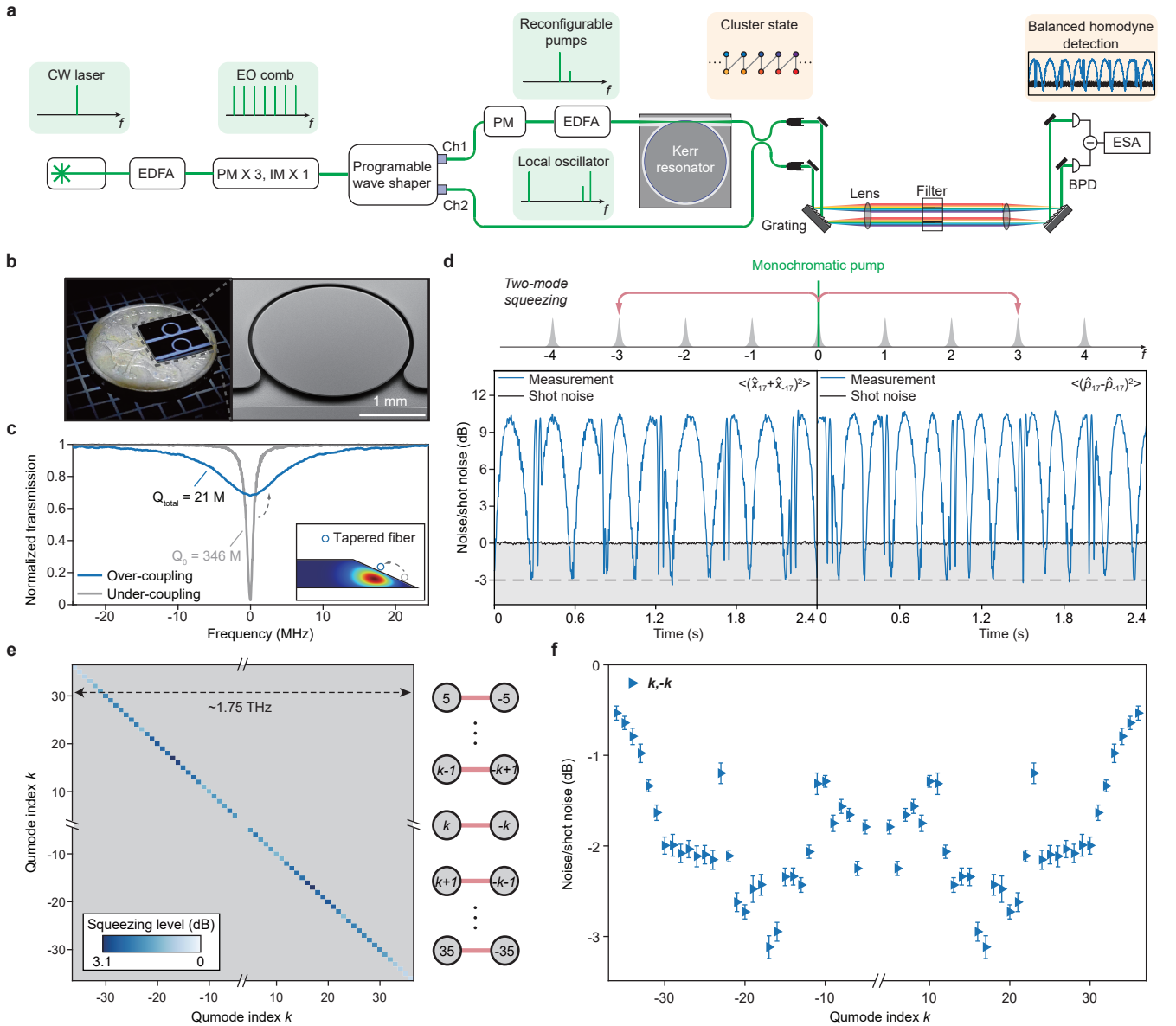


Fig. 2. Experimental setup and performance benchmark. **a**, Experimental setup. CW laser: Continuous-wave laser; EO comb: Electro-optic comb; EDFA: Erbium-doped fiber amplifier; PM: Phase modulator; IM: Intensity modulator; BPD: Balanced photodetector; ESA: Electrical spectrum analyzer. **b**, Left panel: Photo image of the microresonators on a coin. Right panel: Scanning-electron-microscopy image of the microresonator. The intrinsic (Q_0) and total (Q_{total}) Q factors are indicated. Inset: Cross-sectional profiles of the microresonator and the optical mode. The location of the tapered fiber coupler is also indicated. **c**, Transmission spectrum of the microresonator. The intrinsic (Q_0) and total (Q_{total}) Q factors are indicated. Inset: Cross-sectional profiles of the microresonator and the optical mode. The location of the tapered fiber coupler is also indicated. **d**, Upper panel: Pumping scheme and FWM processes. Lower panel: Electrical spectra showing quadrature noise variance (blue) relative to shot noise (gray) for the qumode pair $(-17, 17)$. The relative phase between the pump and the LO is scanned over time. The dashed black line indicates 3 dB below the shot noise. All measurements are taken at 0.5 MHz frequency, 100 kHz resolution bandwidth, and 100 Hz video bandwidth. **e**, Maximal raw squeezing of the quadrature noise variance for different qumode pairs. Measurements in the gray shades are not taken. The right panel shows the entanglement structures. **f**, Maximal raw squeezing of the quadrature noise variance for qumode pairs $(k, -k)$.

yields their variance. A measurement without input from the cluster state is also performed to reveal the shot noise of the LO, based on which the squeezing levels are calculated. Further details of the experimental setup are provided in the Methods and Extended Data Fig. 1.

The microresonator, a silica disk fabricated on a silicon chip⁶⁶ (Fig. 2b), has a lithographically set diameter of 2.6 mm, resulting in a free spectral range (FSR) of approximately 25 GHz. Coupled via a tapered fiber coupler, the microresonator achieves an intrinsic Q ex-

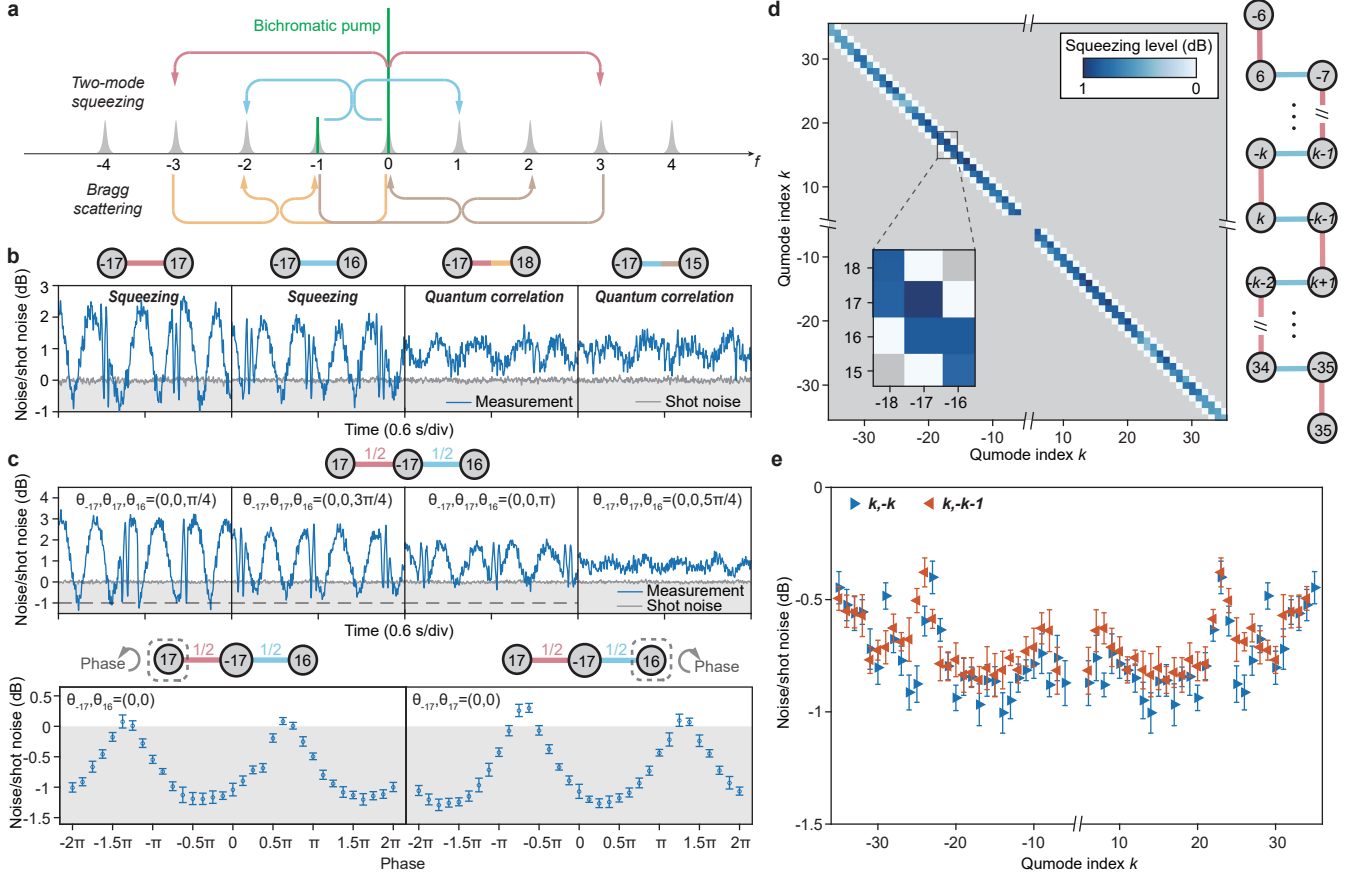


Fig. 3. CV cluster states generated by bichromatic pump lasers. **a**, Pumping scheme and FWM processes. The power ratio of the pump lasers launched at modes 0 and -1 is 1:0.2. **b**, Electrical spectra showing 2-mode quadrature noise variance (blue) relative to shot noise (gray) for representative qumode pairs. The color of the connecting edges corresponds to the FWM processes shown in **a**. The relative phase between the pump and the LO is scanned over time. **c**, Upper panel: Electrical spectra showing 3-mode quadrature noise variance (blue) relative to shot noise (gray). The relative phase between the pump and the LO is scanned over time. The phases assigned to each mode in the LO (θ) are indicated. Lower panel: Minimal quadrature noise variance normalized to shot noise when varying the phases of a mode in the LO. **d**, Maximal two-mode raw squeezing. Measurements in the gray shades are not taken. The right panel shows the graph structure. **e**, Maximal two-mode raw squeezing for qumode pairs $(k, -k)$ and $(k, -k-1)$. All measurements are taken at 0.5 MHz frequency, with 100 kHz resolution bandwidth and 100 Hz video bandwidth.

ceeding 300 million, as determined from the transmitted signal (Fig. 2c). To efficiently extract the cluster state, the relative position between the fiber taper and the microresonator is finely tuned to achieve an over-coupling condition. With a total Q of 21 million, the extraction efficiency is calculated to be 94%. The tapered fiber coupling also ensures uniform over-coupling within the 20 nm wavelength span (Extended Data Fig. 2). Considering additional parasitic losses during filtering and detection, the overall detection efficiency of our system is estimated to be 68.7% (see Methods for details).

To evaluate the performance of our experimental setup, we conduct two-mode squeezing tests using a monochromatic pump laser. Specifically, we pump the microresonator at approximately 1550.06 nm and set the pump power close to the parametric oscillation threshold of

54.25 mW. To measure the quadrature noise variance of $\hat{x}_m + \hat{x}_n$ and $\hat{p}_m - \hat{p}_n$, the LO is configured to provide sidebands at modes m and n with equal power. However, phase drift (ψ) between the two arms of the interferometer prevents deterministic assessment of the two quadratures, since the \hat{x} (\hat{p}) quadratures are transformed to $\hat{x} \cos \psi + \hat{p} \sin \psi$ ($\hat{p} \cos \psi - \hat{x} \sin \psi$). We address this by applying a periodic ramp voltage to a phase modulator inserted before the microresonator, varying ψ to access all quadratures in each measurement. Figure 2d presents the electrical spectra showing the quadrature noise variance for qumodes $(-17, 17)$, normalized to the shot noise. The noise varies periodically due to the applied phase scanning, with the lowest (highest) level indicating the measurement of the maximally squeezed (anti-squeezed) quadratures. We assign the maximally squeezed quadra-

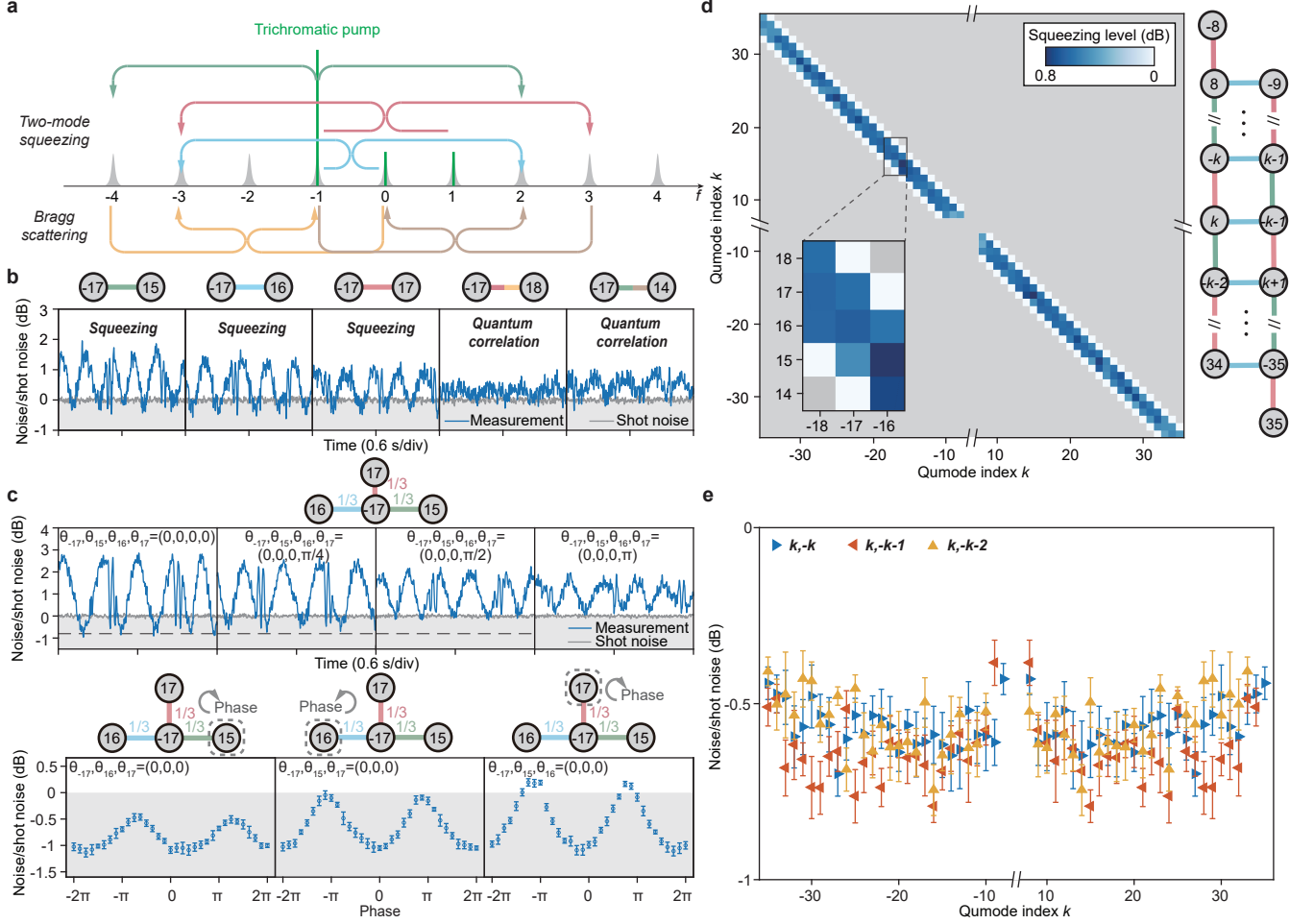


Fig. 4. CV cluster states generated by trichromatic pump lasers. **a**, Pumping scheme and FWM processes. The power ratio of the pump lasers launched at modes -1, 0, and 1 is 1:0.2:0.16, with the phases of the three pump lasers set to be equal. **b**, Electrical spectra showing 2-mode quadrature noise variance (blue) relative to shot noise (gray) for representative qumode pairs. The color of the connecting edges corresponds to the FWM processes shown in **a**. The relative phase between the pump and the LO is scanned over time. **c**, Upper panel: Electrical spectra showing 4-mode quadrature noise variance (blue) relative to shot noise (gray). The relative phase between the pump and the LO is scanned over time. The phases assigned to each mode in the LO (θ) are indicated. Lower panel: Minimal quadrature noise variance normalized to shot noise when varying the phases of a mode in the LO. **d**, Maximal two-mode raw squeezing. Measurements in the gray shades are not taken. The right panel shows the graph structure. **e**, Maximal two-mode raw squeezing for qumode pairs $(k, -k)$, $(k, -k-1)$, and $(k, -k-2)$. All measurements are taken at 0.5 MHz frequency, with 100 kHz resolution bandwidth and 100 Hz video bandwidth.

tures to $\hat{x}_{17} + \hat{x}_{-17}$ and $\hat{p}_{17} - \hat{p}_{-17}$. The raw squeezing is calculated by comparing the lowest quadrature noise variance of 30 independent measurements with the shot noise level, reaching 3.12 ± 0.13 dB and 3.05 ± 0.10 dB for $\hat{x}_{17} + \hat{x}_{-17}$ and $\hat{p}_{17} - \hat{p}_{-17}$, respectively. By correcting the electrical noise of the photodetector, these values improve to 3.23 ± 0.13 dB and 3.17 ± 0.10 dB.

Within the 1.75-THz optical span of the EO comb, we measure the quadrature noise variance of 31 qumode pairs (Fig. 2e). Considerable raw squeezing is observed for qumodes with opposite indices, from which the entanglement structures are inferred to be pair-like. The raw squeezing for different qumode pairs is summarized in Fig. 2f, with spectral dependence primarily attributed to

the parametric gain. However, the raw squeezing around qumodes $(-23, 23)$ exhibited abnormal degradation, attributed to avoided mode crossing caused by the coupling with other transverse mode families co-existing in the microresonator⁴⁹ (Extended Data Fig. 2).

CV cluster states with bichromatic pump

We investigate the excitation of cluster states using bichromatic pump lasers. Extended Data Fig. 3 illustrates two-mode squeezing structures for several pump configurations. When the secondary pump power is set to 1/5 of the primary pump, squeezing occurs for qumode pairs with indices summing to 0 or -1. This pattern exhibits a more uniform distribution of squeezing compared to other configurations, attributed to the comparable

nonlinear coupling strengths of the two squeezing operations (Fig. 3a). Experimentally, this configuration allows for higher power input into the microresonator without generating undesirable sidebands than setting the secondary pump power to 1/4 of the primary pump.

We further characterize two-mode squeezing by evaluating the noise variance of $\hat{x}_m + \hat{x}_n$ (Fig. 3b). Two-mode squeezing is observed for the qumodes (17, -17) and (16, -17), directly resulting from the squeezing operations. The quadrature noise variance for the qumodes (18, -17) and (15, -17), although remaining above the shot noise limit, exhibits phase-dependent behavior. This quantum correlation arises from Bragg scattering, described by the Hamiltonian $-2gA_0A_{-1}^*\hat{a}_{-k+1}^\dagger\hat{a}_{-k} + \text{h.c.}$. Although Bragg scattering does not directly induce squeezing, it synergizes with two-mode squeezing operations between the qumodes $(-k, k)$ to induce effective squeezing between the otherwise uncorrelated $(k, -k+1)$. These mechanisms also lead to quantum correlations observed in the qumodes $(k, -k-2)$, with additional contributions from the squeezing solely provided by A_{-1} . These cascaded nonlinear effects are weaker than direct two-mode squeezing operations, with further cascading having a negligible impact (Extended Data Fig. 4).

We also measure the quadrature noise variances for three qumodes and observe quantum interference with respect to their phase relations (Fig. 3c). If their phases are aligned, the quadrature yields $\hat{x}_{-17} + (\hat{x}_{17} + \hat{x}_{16})/2$. Significant raw squeezing is achieved for appropriate phase relations between these qumodes, which vanishes if their phases are altered. Notably, the maximum three-mode raw squeezing (1.29 ± 0.10 dB) surpasses that of any related two-mode squeezing (< 1 dB), which indicates tri-mode entanglement.

Figure 3d shows two-mode squeezing measurements for selected pairs of qumodes. Consistent with our theoretical predictions, squeezing is observed exclusively for qumode pairs with indices summing to 0 and -1. Each qumode is entangled with two others, forming a chain-like one-dimensional structure. The fully-connected cluster state extends from qumode ± 6 to ± 35 , encompassing 60 qumodes. The raw squeezing for selected qumode pairs is summarized in Fig. 3e, typically ranging from 0.5 dB to 0.9 dB, showing a relatively even distribution over the spectrum. The maximum raw squeezing observed is 1 dB.

CV cluster states with trichromatic pump

To generate CV cluster states with more complex structures, we employ trichromatic pump lasers at mode indices $(-1, 0, 1)$, with relative power set to 1:0.2:0.16 and equal phases. This configuration induces five primary FWM processes, including three squeezing and two Bragg scattering operations (Fig. 4a). We present several two-mode quadrature noise variances related to qumode -17. As depicted in Fig. 4b, the squeezing operations induce two-mode squeezing for qumodes (17, -17), (16, -17), and (15, -17). Additionally, quantum correlation without squeezing is observed for qumodes (18, -17) and

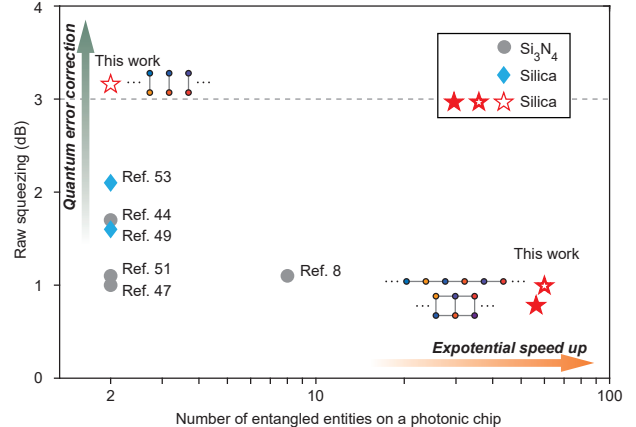


Fig. 5. Comparison of raw squeezing and number of entangled entities between CV quantum states generated on photonic chips. The dashed line indicates 3 dB raw squeezing. Results obtained in Si₃N₄ microresonators^{8,44,47,51} and silica microresonators^{49,53} are plotted for comparison.

(14, -17) due to cascaded nonlinear interactions involving two-mode squeezing and Bragg scattering. This quantum correlation vanishes quickly for an increased number of involved FWM processes (Extended Data Fig. 5).

Figure 4c presents measurements of the four-mode quadrature noise variances. Here the quadrature yields $\hat{x}_{-17} + (\hat{x}_{15} + \hat{x}_{16} + \hat{x}_{17})/3$ for aligned phases, and the raw squeezing is observed to vary according to their phase relations. The maximum four-mode raw squeezing (1.13 ± 0.08 dB) is larger than that of any related two-mode squeezing (< 0.8 dB), indicating four-mode entanglement.

Figure 4d showcases a comprehensive characterization of two-mode squeezing. Squeezing is observed exclusively for qumode pairs with indices summing to 0, -1, and -2. Thus, the entanglement structure forms a two-dimensional rail, with each qumode connecting to three other qumodes. The fully-connected cluster state extends from qumode ± 8 to ± 35 , encompassing 56 qumodes in total. The raw squeezing for selected qumode pairs is evenly distributed across the spectrum, with a maximum level reaching 0.8 dB (Fig. 4e).

Discussion

Accomplishing practical quantum tasks, such as fault-tolerant quantum computation, necessitates a substantial number of entangled entities to facilitate exponential speedup and a high level of raw squeezing for effective quantum error correction^{16,19,54}. Figure 5 compares the number of entangled entities and raw squeezing levels across various photonic-chip-based CV quantum systems. Our 60 entangled spectral qumodes represent the largest CV cluster states generated on a photonic chip to date. Complete characterization of the covariance matrices is required to reveal the actual graph structures of

the cluster state⁶⁷. Nevertheless, the 3 dB raw squeezing observed in the two-mode systems of this work marks a significant step towards meeting the genuine van Loock-Furusawa inseparability criterion for multipartite entangled systems⁶⁸.

Further improvements in our system are feasible. Due to dispersion, microresonator modes may not perfectly align with the qumodes, limiting resonantly-enhanced nonlinear interactions across a broader spectral range. Dispersion engineering, initially developed for broadband classical microcombs⁶³, can be adapted to quantum microcombs to extend the gain bandwidth of parametric processes. Effective filtering of higher-order transverse modes, which prevents squeezing degradation due to avoided mode crossings, can be achieved by optimizing the cross-sectional geometries of microresonators^{69,70}. These approaches are underway to develop larger-scale cluster states.

Advanced photonic integration is expected to leverage the raw squeezing achieved. For example, current silicon photonic technologies have enabled the heterogeneous integration of photodetectors with photonic circuitry^{50,71}, eliminating loss during off-chip detection. Integration with other photonic components such as high-speed modulators⁷², microcomb-based LOs^{63,73}, and spectral shapers⁷⁴ would facilitate the creation, control, and detection of spectral CV cluster states on a single photonic chip. We envision that chip-based CV cluster states with sufficient raw squeezing would become the cornerstone for quantum networks with improved robustness, quantum measurements with enhanced precision⁵⁵⁻⁵⁷, and quantum computers with explicit quantum advantages^{9,10}.

Methods

Experimental details. The detailed experimental setup is shown in Extended Data Fig. 1. The continuous-wave laser operates at approximately 1550.06 nm (New Focus, TLB-6700). A microwave generator (Keysight PSG E8257D) provides low-noise 25-GHz microwave signals, which are amplified to drive the modulators. For phase modulation, microwave signal phases are adjusted to achieve the broadest spectrum, while for intensity modulation, microwave phases and DC bias are optimized to flatten the comb spectrum. The EO comb power is tapped using a 90/10 fiber directional coupler, with 10% of the power monitored via a photodetector for servo-locking the DC bias of the intensity modulator, ensuring long-term stability. A multi-channel waveshaper (II-IV waveshaper 4000A) synthesizes the pump and LO from the EO comb.

The pump is amplified using an EDFA, with amplified spontaneous emission noise collectively filtered by a fixed-wavelength wavelength division multiplexer and a tunable bandpass filter. The transmitted optical signal from the microresonator is tapped using a 99/1 fiber directional coupler, with 1% of the light monitored by a photodetector. This signal is used to feedback control the pump laser frequency to sustain long-term operations.

The LO is amplified using an EDFA and is then combined with the transmitted signal from the microresonator via a 50/50 fiber directional coupler, achieving a high interference efficiency of 99.7%. To minimize dispersion effects, the temporal waveforms of the EO comb at the coupler input are interrogated using an autocorrelator. Proper group velocity dispersion applied via the waveshaper ensures the minimal temporal width of the EO comb, indicating equal phases of all comb lines. After calibrating the dispersion,

assessment of the \hat{x} and \hat{p} quadratures are enabled by applying additional phases onto selected comb lines using the waveshaper.

A homemade tunable filter, consisting of two gratings and two lenses, is designed to filter out the residual pump. Combined signals are directed into free space using collimators and separated spatially by the grating. The residual pump is blocked by spatial filters, retaining high transmittance (>90%) of other wavelengths. The remaining light is received by a high-quantum efficiency (92.5%) homemade balanced photodetector (Fermionics, FD500N-1550), whose noise performance is characterized in Extended Data Fig. 1c. The balanced photodetector operates in the shot-noise limited regime with an input power greater than 2 mW and exhibits a common-mode noise rejection of 35 dB. All electrical spectra are recorded using an ESA (Rohde & Schwarz FPL1206).

The detection efficiency in our system accounting for the 18.5% optical loss, 92.5% photodiode quantum efficiency, and 97% transmission of the tapered fiber, is 73.1%.

Device fabrication. The fabrication process of the silica microresonator has been outlined in detail elsewhere⁶⁶. The microresonators are fabricated on a high-resist silicon wafer with an 8-micron-thick thermally oxidized silica film. Initially, the wafer is spin-coated with a photoresist (S1813) of nominal 1.4-micron thickness, followed by UV lithography using a contact mask aligner (SUSS MA6). Subsequently, the photoresist patterns are transferred to the underlying silica film through a wet etching process using buffered oxide etchant for 150 minutes. After removing the photoresist, the silicon substrate is etched using XeF₂ gas to suspend the disk structure. Finally, the microresonator is annealed in a flowing argon environment at 950 degrees for 30 minutes using a rapid thermal annealer. This annealing step reduces absorption losses and improves the Q of the microresonator.

Theoretical model. We present the theoretical model used to calculate the quadrature noise variance for the exemplary case of the bichromatic pump. The equations of motion for the annihilation operator of the k_{th} qumode, \hat{a}_k , are described by a set of coupled-mode equations⁷⁵:

$$\begin{aligned} \frac{d\hat{a}_k}{dt} = & - \left(\frac{\kappa}{2} + i\zeta_k - 2ig|A_0|^2 - 2ig|A_{-1}|^2 \right) \hat{a}_k \\ & + ig(A_0A_0\hat{a}_{-k}^\dagger + 2A_0A_{-1}\hat{a}_{-k-1}^\dagger + A_{-1}A_{-1}\hat{a}_{-k-2}^\dagger) \quad (2) \\ & + 2ig(A_0^*A_{-1}\hat{a}_{k+1} + A_{-1}^*A_0\hat{a}_{k-1}) \\ & + \sqrt{\kappa_0}\hat{V}_{0,k} + \sqrt{\kappa_e}\hat{V}_{e,k}, \end{aligned}$$

Here, κ , κ_0 , and κ_e represent the total, intrinsic, and external coupling loss rates of the microresonator, respectively. The frequency misalignment between the k_{th} qumode and the nearest microresonator mode is denoted by ζ_k , which equals $\zeta_0 + \frac{1}{2}D_2k^2$, accounting for the pump-cavity detuning at the 0_{th} mode and the second-order dispersion of the microresonator (D_2). A_0 and A_{-1} are the classical coherent fields of modes 0 and -1. The vacuum fluctuations arising from the intrinsic and external coupling loss channels are denoted by Langevin operators $\hat{V}_{0,k}$ and $\hat{V}_{e,k}$, respectively, and are fully uncorrelated. They are normalized such that

$$[\hat{V}_{0,k}(t), \hat{V}_{0,k'}^\dagger(t')] = [\hat{V}_{e,k}(t), \hat{V}_{e,k'}^\dagger(t')] = \delta_{k,k'}\delta(t-t') \quad (3)$$

$$[\hat{V}_{0,k}^\dagger(t), \hat{V}_{0,k'}(t')] = [\hat{V}_{e,k}^\dagger(t), \hat{V}_{e,k'}(t')] = 0 \quad (4)$$

$$[\hat{V}_{0,k}(t), \hat{V}_{0,k'}(t')] = [\hat{V}_{e,k}(t), \hat{V}_{e,k'}(t')] = 0 \quad (5)$$

$$[\hat{V}_{0,k}(t), \hat{V}_{e,k'}^\dagger(t')] = [\hat{V}_{0,k}^\dagger(t), \hat{V}_{e,k'}(t')] = [\hat{V}_{0,k}(t), \hat{V}_{e,k'}(t')] = 0 \quad (6)$$

Fourier transforming equation (2) yields the solution of \hat{a}_k in the frequency domain, represented as $\hat{a}_k = \int \hat{\tilde{a}}_k(\omega)e^{-i\omega t}d\omega$. The Fourier frequency ω is directly related to the frequency offset of the electrical spectral analyzer. The state collected at the output port of the waveguide coupler is derived using the input-output relation of the microresonator:

$$\hat{a}_k^{\text{out}} = \sqrt{\kappa_e}\hat{a}_k - \hat{V}_{e,k}. \quad (7)$$

Including the total detection efficiency of our system (η), the state received at the detector is given by:

$$\hat{a}_k^{\text{det}} = \sqrt{\eta}\hat{a}_k^{\text{out}} + \sqrt{1-\eta}\hat{V}_{l,k}, \quad (8)$$

where $\hat{V}_{l,k}$ denotes another vacuum fluctuation source that is uncorrelated with $\hat{V}_{0,k}$ and $\hat{V}_{e,k}$. Finally, The quadrature noise variance is calculated from the detected field operators based on the commutation relations of the vacuum fluctuation operators.

-
- [1] Montanaro, A. Quantum algorithms: an overview. *npj Quan. Info.* **2**, 1–8 (2016).
- [2] Kempe, J. Multiparticle entanglement and its applications to cryptography. *Phys. Rev. A* **60**, 910 (1999).
- [3] Kimble, H. J. The quantum internet. *Nature* **453**, 1023–1030 (2008).
- [4] Yokoyama, S. *et al.* Ultra-large-scale continuous-variable cluster states multiplexed in the time domain. *Nat. Photon.* **7**, 982–986 (2013).
- [5] Chen, M., Menicucci, N. C. & Pfister, O. Experimental realization of multipartite entanglement of 60 modes of a quantum optical frequency comb. *Phys. Rev. Lett.* **112**, 120505 (2014).
- [6] Asavanant, W. *et al.* Generation of time-domain-multiplexed two-dimensional cluster state. *Science* **366**, 373–376 (2019).
- [7] Larsen, M. V., Guo, X., Breum, C. R., Neergaard-Nielsen, J. S. & Andersen, U. L. Deterministic generation of a two-dimensional cluster state. *Science* **366**, 369–372 (2019).
- [8] Arrazola, J. M. *et al.* Quantum circuits with many photons on a programmable nanophotonic chip. *Nature* **591**, 54–60 (2021).
- [9] Zhong, H.-S. *et al.* Quantum computational advantage using photons. *Science* **370**, 1460–1463 (2020).
- [10] Madsen, L. S. *et al.* Quantum computational advantage with a programmable photonic processor. *Nature* **606**, 75–81 (2022).
- [11] Horodecki, R., Horodecki, P., Horodecki, M. & Horodecki, K. Quantum entanglement. *Rev. Mod. Phys.* **81**, 865 (2009).
- [12] Einstein, A., Podolsky, B. & Rosen, N. Can quantum-mechanical description of physical reality be considered complete? *Phys. Rev.* **47**, 777 (1935).
- [13] Schrödinger, E. Discussion of probability relations between separated systems. In *Proc. Camb. Phil. Soc.*, vol. 31, 555–563 (Cambridge University Press, 1935).
- [14] Raussendorf, R. & Briegel, H. J. A one-way quantum computer. *Phys. Rev. Lett.* **86**, 5188 (2001).
- [15] Raussendorf, R., Browne, D. E. & Briegel, H. J. Measurement-based quantum computation on cluster states. *Phys. Rev. A* **68**, 022312 (2003).
- [16] Menicucci, N. C. *et al.* Universal quantum computation with continuous-variable cluster states. *Phys. Rev. Lett.* **97**, 110501 (2006).
- [17] Raussendorf, R., Harrington, J. & Goyal, K. Topological fault-tolerance in cluster state quantum computation. *New J. Phys.* **9**, 199 (2007).
- [18] Gu, M., Weedbrook, C., Menicucci, N. C., Ralph, T. C. & van Loock, P. Quantum computing with continuous-variable clusters. *Phys. Rev. A* **79**, 062318 (2009).
- [19] Menicucci, N. C. Fault-tolerant measurement-based quantum computing with continuous-variable cluster states. *Phys. Rev. Lett.* **112**, 120504 (2014).
- [20] Furusawa, A. *et al.* Unconditional quantum teleportation. *Science* **282**, 706–709 (1998).
- [21] Zhong, H.-S. *et al.* 12-photon entanglement and scalable scattershot boson sampling with optimal entangled-photon pairs from parametric down-conversion. *Phys. Rev. Lett.* **121**, 250505 (2018).
- [22] Wang, X.-L. *et al.* 18-qubit entanglement with six photons’ three degrees of freedom. *Phys. Rev. Lett.* **120**, 260502 (2018).
- [23] Braunstein, S. L. & Van Loock, P. Quantum information with continuous variables. *Rev. Mod. Phys.* **77**, 513 (2005).
- [24] Weedbrook, C. *et al.* Gaussian quantum information. *Rev. Mod. Phys.* **84**, 621 (2012).
- [25] Pysher, M., Miwa, Y., Shahrokshahi, R., Bloomer, R. & Pfister, O. Parallel generation of quadripartite cluster entanglement in the optical frequency comb. *Phys. Rev. Lett.* **107**, 030505 (2011).
- [26] Pinel, O. *et al.* Generation and characterization of multimode quantum frequency combs. *Phys. Rev. Lett.* **108**, 083601 (2012).
- [27] Roslund, J., De Araujo, R. M., Jiang, S., Fabre, C. & Treps, N. Wavelength-multiplexed quantum networks with ultrafast frequency combs. *Nat. Photon.* **8**, 109–112 (2014).
- [28] Cai, Y. *et al.* Multimode entanglement in reconfigurable graph states using optical frequency combs. *Nat. Commun.* **8**, 15645 (2017).
- [29] Menicucci, N. C. Temporal-mode continuous-variable cluster states using linear optics. *Phys. Rev. A* **83**, 062314 (2011).
- [30] Alexander, R. N., Yokoyama, S., Furusawa, A. & Menicucci, N. C. Universal quantum computation with temporal-mode bilayer square lattices. *Phys. Rev. A* **97**, 032302 (2018).
- [31] Su, D. *et al.* Implementing quantum algorithms on temporal photonic cluster states. *Phys. Rev. A* **98**, 032316 (2018).
- [32] Yoshikawa, J.-i. *et al.* Invited article: Generation of one-million-mode continuous-variable cluster state by unlimited time-domain multiplexing. *APL Photon.* **1** (2016).
- [33] Su, X. *et al.* Gate sequence for continuous variable one-way quantum computation. *Nat. Commun.* **4**, 2828 (2013).
- [34] Armstrong, S. *et al.* Programmable multimode quantum networks. *Nat. Commun.* **3**, 1026 (2012).
- [35] Zhang, K. *et al.* Reconfigurable hexapartite entanglement by spatially multiplexed four-wave mixing processes. *Phys. Rev. Lett.* **124**, 090501 (2020).
- [36] Wang, J., Sciarrino, F., Laing, A. & Thompson, M. G. Integrated photonic quantum technologies. *Nat. Photon.* **14**, 273–284 (2020).
- [37] Elshaari, A. W., Pernice, W., Srinivasan, K., Benson, O. & Zwiller, V. Hybrid integrated quantum photonic circuits. *Nat. Photon.* **14**, 285–298 (2020).
- [38] Kanter, G. S. *et al.* Squeezing in a LiNbO₃ integrated optical waveguide circuit. *Opt. Express* **10**, 177–182 (2002).
- [39] Stefszky, M. *et al.* Waveguide cavity resonator as a source

- of optical squeezing. *Phys. Rev. Appl.* **7**, 044026 (2017).
- [40] Lenzini, F. *et al.* Integrated photonic platform for quantum information with continuous variables. *Sci. Adv.* **4**, eaat9331 (2018).
- [41] Kashiwazaki, T. *et al.* Continuous-wave 6-db-squeezed light with 2.5-thz-bandwidth from single-mode ppln waveguide. *APL Photon.* **5** (2020).
- [42] Nehra, R. *et al.* Few-cycle vacuum squeezing in nanophotonics. *Science* **377**, 1333–1337 (2022).
- [43] Fürst, J. *et al.* Quantum light from a whispering-gallery-mode disk resonator. *Phys. Rev. Lett.* **106**, 113901 (2011).
- [44] Dutt, A. *et al.* On-chip optical squeezing. *Phys. Rev. Appl.* **3**, 044005 (2015).
- [45] Otterpohl, A. *et al.* Squeezed vacuum states from a whispering gallery mode resonator. *Optica* **6**, 1375–1380 (2019).
- [46] Zhao, Y. *et al.* Near-degenerate quadrature-squeezed vacuum generation on a silicon-nitride chip. *Phys. Rev. Lett.* **124**, 193601 (2020).
- [47] Vaidya, V. D. *et al.* Broadband quadrature-squeezed vacuum and nonclassical photon number correlations from a nanophotonic device. *Sci. Adv.* **6**, eaba9186 (2020).
- [48] Zhang, Y. *et al.* Squeezed light from a nanophotonic molecule. *Nat. Commun.* **12**, 2233 (2021).
- [49] Yang, Z. *et al.* A squeezed quantum microcomb on a chip. *Nat. Commun.* **12**, 4781 (2021).
- [50] Tasker, J. F. *et al.* Silicon photonics interfaced with integrated electronics for 9 ghz measurement of squeezed light. *Nat. Photon.* **15**, 11–15 (2021).
- [51] Jahanbozorgi, M. *et al.* Generation of squeezed quantum microcombs with silicon nitride integrated photonic circuits. *Optica* **10**, 1100–1101 (2023).
- [52] Park, T. *et al.* Single-mode squeezed-light generation and tomography with an integrated optical parametric oscillator. *Sci. Adv.* **10**, ead1814 (2024).
- [53] Yang, Z. *et al.* A quantum microcomb with 2.1 db raw squeezing. In *2022 Conference on Lasers and Electro-Optics (CLEO)*, 1–2 (2022).
- [54] Lloyd, S. & Braunstein, S. L. Quantum computation over continuous variables. *Phys. Rev. Lett.* **82**, 1784 (1999).
- [55] Aasi, J. *et al.* Enhanced sensitivity of the ligo gravitational wave detector by using squeezed states of light. *Nat. Photon.* **7**, 613–619 (2013).
- [56] Li, B.-B. *et al.* Quantum enhanced optomechanical magnetometry. *Optica* **5**, 850–856 (2018).
- [57] Shi, H., Zhang, Z., Pirandola, S. & Zhuang, Q. Entanglement-assisted absorption spectroscopy. *Phys. Rev. Lett.* **125**, 180502 (2020).
- [58] Vahlbruch, H., Mehmet, M., Danzmann, K. & Schnabel, R. Detection of 15 db squeezed states of light and their application for the absolute calibration of photoelectric quantum efficiency. *Phys. Rev. Lett.* **117**, 110801 (2016).
- [59] Menicucci, N. C., Flammia, S. T. & Pfister, O. One-way quantum computing in the optical frequency comb. *Phys. Rev. Lett.* **101**, 130501 (2008).
- [60] Diddams, S. A., Vahala, K. & Udem, T. Optical frequency combs: Coherently uniting the electromagnetic spectrum. *Science* **369**, eaay3676 (2020).
- [61] Kippenberg, T., Spillane, S. & Vahala, K. Kerr-nonlinearity optical parametric oscillation in an ultrahigh-q toroid microcavity. *Phys. Rev. Lett.* **93**, 083904 (2004).
- [62] Kippenberg, T. J., Holzwarth, R. & Diddams, S. Microresonator-based optical frequency combs. *Science* **332**, 555–559 (2011).
- [63] Kippenberg, T. J., Gaeta, A. L., Lipson, M. & Gorodetsky, M. L. Dissipative Kerr solitons in optical microresonators. *Science* **361** (2018).
- [64] Kues, M. *et al.* Quantum optical microcombs. *Nature Photonics* **13**, 170–179 (2019).
- [65] Murata, H., Morimoto, A., Kobayashi, T. & Yamamoto, S. Optical pulse generation by electrooptic-modulation method and its application to integrated ultrashort pulse generators. *IEEE J. Sel. Top. Quantum Electron.* **6**, 1325–1331 (2000).
- [66] Lee, H. *et al.* Chemically etched ultrahigh-q wedge-resonator on a silicon chip. *Nat. Photon.* **6**, 369–373 (2012).
- [67] Menicucci, N. C., Flammia, S. T. & van Loock, P. Graphical calculus for gaussian pure states. *Phys. Rev. A* **83**, 042335 (2011).
- [68] Van Loock, P. & Furusawa, A. Detecting genuine multipartite continuous-variable entanglement. *Phys. Rev. A* **67**, 052315 (2003).
- [69] Kordts, A., Pfeiffer, M. H., Guo, H., Brasch, V. & Kippenberg, T. J. Higher order mode suppression in high-q anomalous dispersion sin microresonators for temporal dissipative kerr soliton formation. *Opt. Lett.* **41**, 452–455 (2016).
- [70] Yang, K. Y. *et al.* Bridging ultrahigh-Q devices and photonic circuits. *Nat. Photon.* **12**, 297 (2018).
- [71] Yu, Q. *et al.* Heterogeneous photodiodes on silicon nitride waveguides. *Opt. Express* **28**, 14824–14830 (2020).
- [72] Wang, C. *et al.* Integrated lithium niobate electro-optic modulators operating at cmos-compatible voltages. *Nature* **562**, 101–104 (2018).
- [73] Yu, M. *et al.* Integrated femtosecond pulse generator on thin-film lithium niobate. *Nature* **612**, 252–258 (2022).
- [74] Wang, J. *et al.* Reconfigurable radio-frequency arbitrary waveforms synthesized in a silicon photonic chip. *Nat. Commun.* **6**, 5957 (2015).
- [75] Chembo, Y. K. Quantum dynamics of Kerr optical frequency combs below and above threshold: Spontaneous four-wave mixing, entanglement, and squeezed states of light. *Phys. Rev. A* **93**, 033820 (2016).

Acknowledgments This work was supported by National Key R&D Plan of China (Grant No. 2021YFB2800601), Beijing Natural Science Foundation (Z210004, Z240007), National Natural Science Foundation of China (92150108, 62222515, 12125402, 12174438), and the High-performance Computing Platform of Peking University. Device fabrication in this work is supported by the Micro/nano Fabrication Laboratory of Synergetic Extreme Condition User Facility (SECUF).

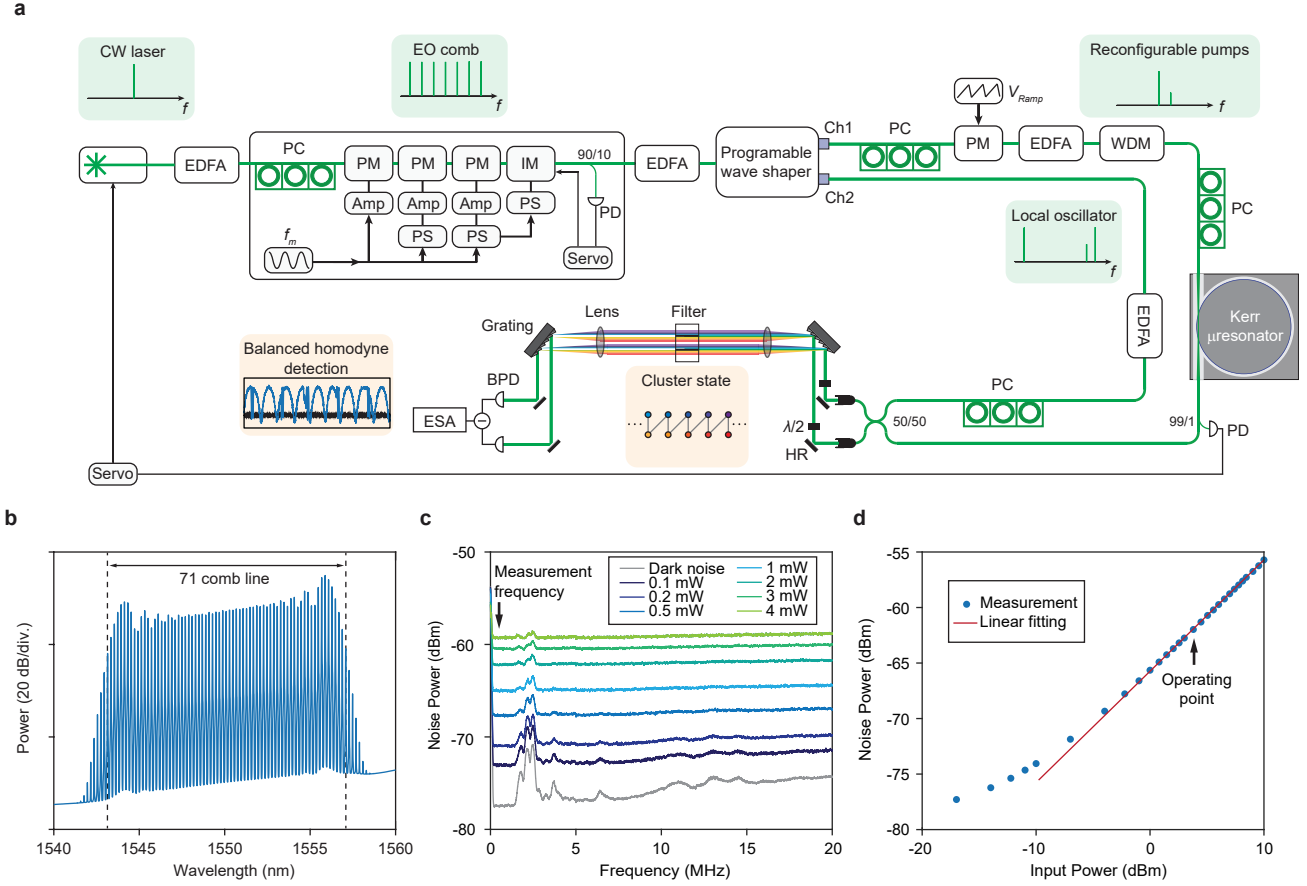
Author contributions The project was conceived by W.Z., K.L., and Q.-F.Y. Experiments were designed and performed by W.Z., K.L., Y.W., and Q.-F.Y. Devices were fabricated by X.Z., Y.C., J.L., Z.L., and B.-B.L. Theory was developed by W.Z., Y.W., B.J., F.S., Q.H., and Q.-F.Y. All authors participated in writing the manuscript.

Competing interests The authors declare no compet-

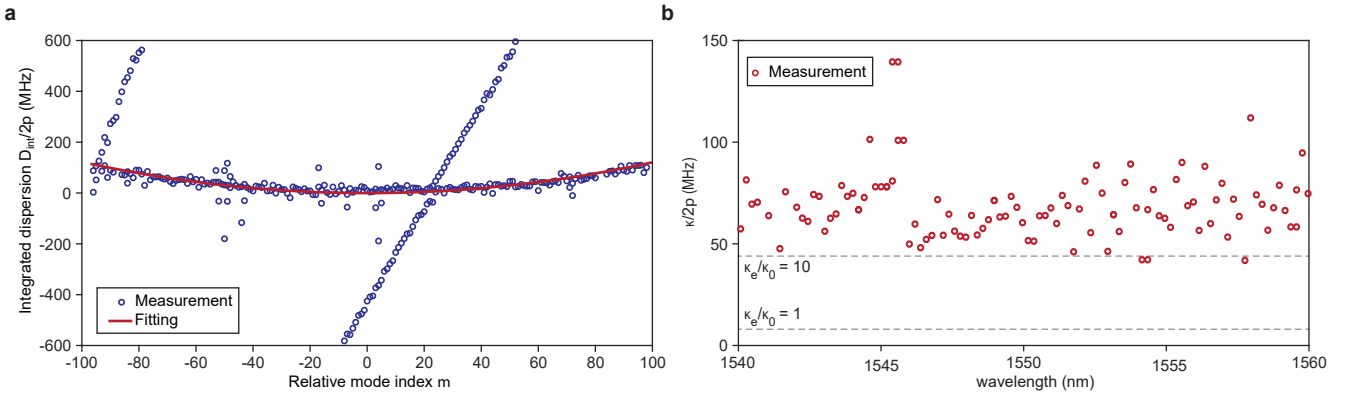
ing interests.

Correspondence and requests for materials should be addressed to K.L., Q.H., B.-B.L., and Q.-F.Y.

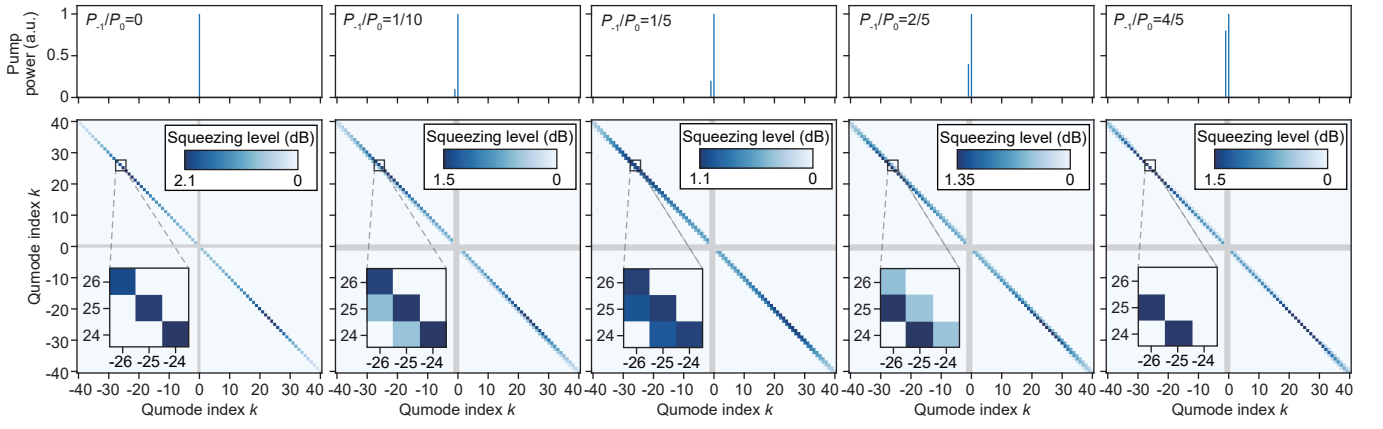
Additional information



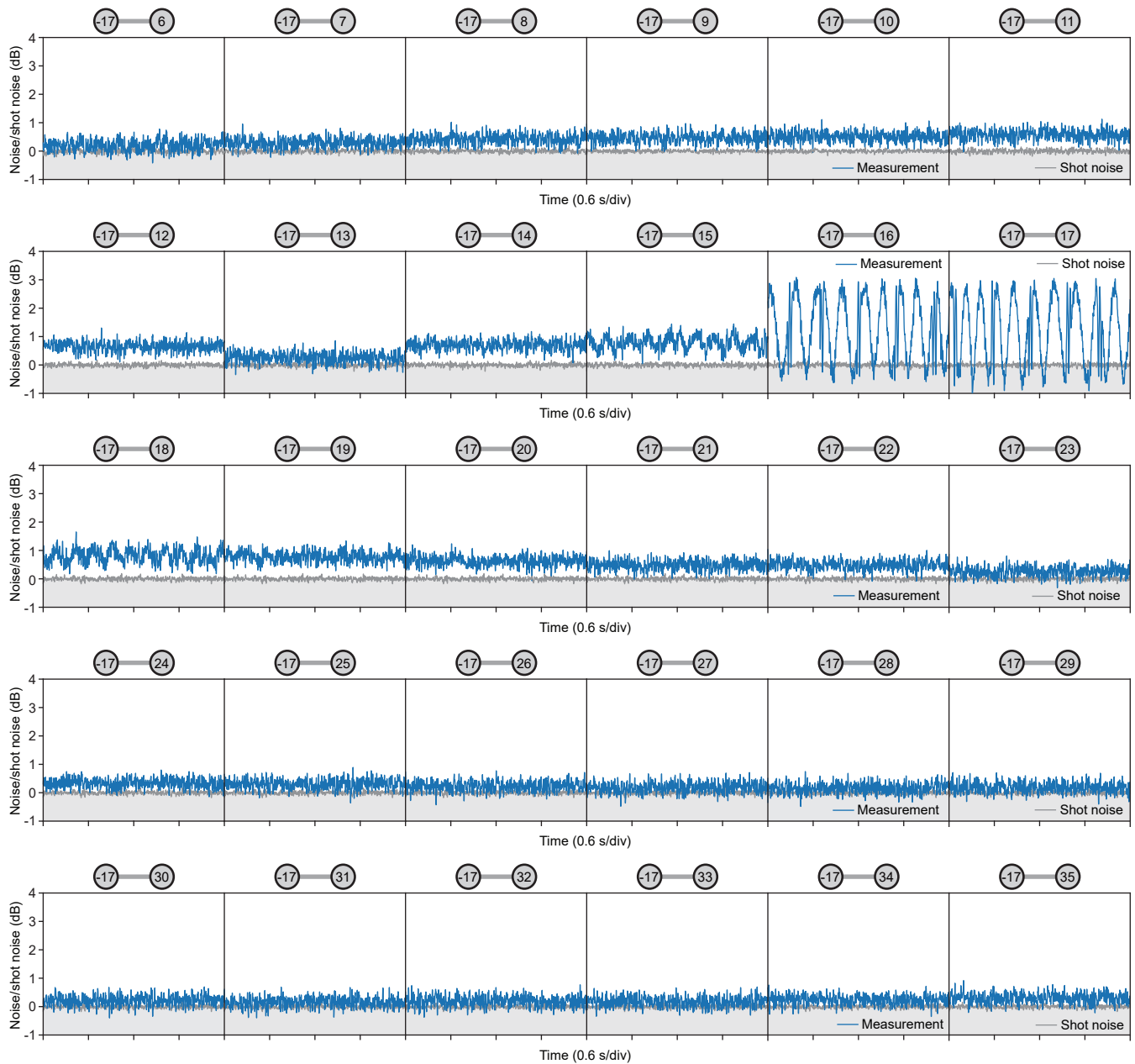
Extended Data Fig. 1. Detailed experimental setup and device performance. **a**, Experimental setup. CW laser: Continuous-wave laser; EO comb: Electro-optic comb; EDFA: Erbium-doped fiber amplifier; PC: Polarization controller; PM: Phase modulator; IM: Intensity modulator; AMP: Electrical amplifier; PS: Electrical phase shifter; WDM: wavelength division multiplexer; HR: mirror with highly-reflective coating; $\lambda/2$: half-wave plate; PD: Photodetector; BPD: Balanced photodetector; ESA: Electrical spectrum analyzer. **b**, Optical spectrum of the EO comb. **c**, Electrical noise spectra of the BPD at different input optical power. **d**, Electrical noise of the BPD at 0.5 MHz as a function of input optical power. The red line indicates the linear operating regime. All measurements are taken with a resolution bandwidth of 100 kHz and a video of 100 Hz.



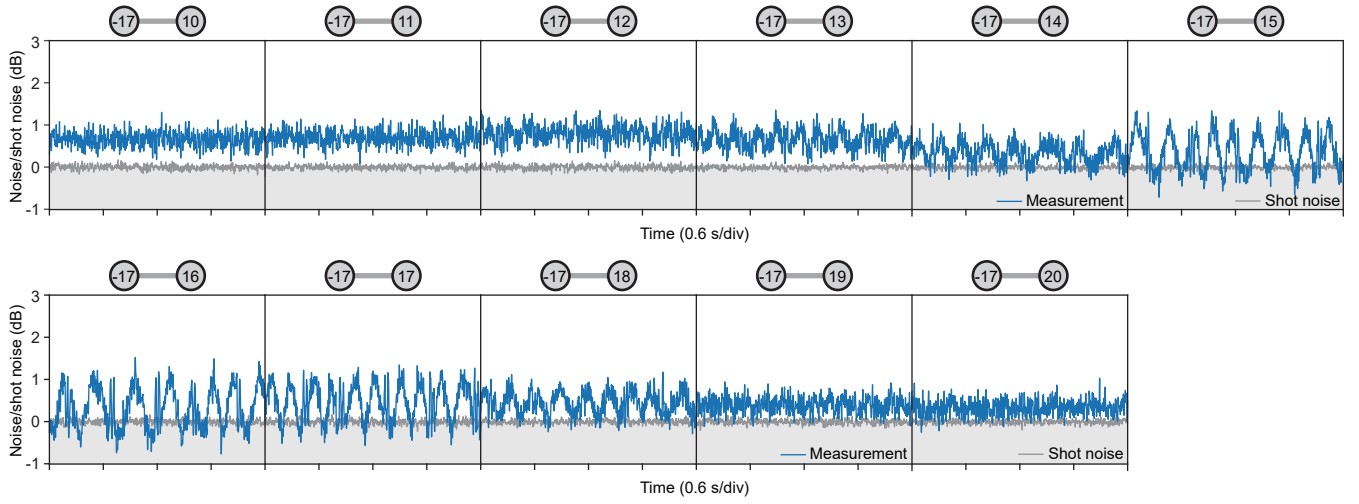
Extended Data Fig. 2. Characterization of the longitudinal mode family. **a**, Mode family dispersion. The integrated dispersion is defined as $D_{\text{int}}(\mu) = \omega_{\mu} - \mu D_1 = D_2 \mu^2 / 2 + \mathcal{O}(\mu^3)$ as a function of mode index μ relative to the pump. ω_{μ} is the resonant frequency of the μ_{th} mode and D_1 is the FSR. The red line denotes parabolic fitting with $D_2/2\pi = 23.9$ kHz. **b**, Distribution of the total loss rates (κ) of the longitudinal mode family versus wavelength. The total loss rate corresponding to critical coupling ($\kappa_e/\kappa_0 = 1$) and strong over-coupling ($\kappa_e/\kappa_0 = 10$) is also indicated.



Extended Data Fig. 3. Simulated two-mode squeezing for different pumping strategies. Upper panel: Optical spectra of the bichromatic pump. From left to right, the power of the secondary pump at mode -1 (P_{-1}) is set to 0, 1/10, 1/5, 2/5, and 4/5 of the primary pump at mode 0 (P_0). Lower panel: simulated two-mode squeezing accounting for experimentally measured cavity escaping and detection efficiencies. The gray shades indicate the qumodes being pumped. Parameters used in the simulations are: $P_0 = 0.5P_{\text{th}}$ (the parametric oscillation threshold $P_{\text{th}} = \kappa^3/(8g\kappa_e\hbar\omega_0)$), $D_2 = 0.0026\kappa$, $\zeta_0 = -\kappa/2$, and Fourier frequency $\omega = 0$.



Extended Data Fig. 4. Additional measurement of two-mode squeezing associated with qumode -17 for the bichromatic pump. Electrical spectra showing 2-mode quadrature noise variance (blue) relative to shot noise (black) for representative qumode pairs. The relative phase between the pump and the LO is scanned over time. All measurements are taken at 0.5 MHz frequency, with 100 kHz resolution bandwidth and 100 Hz video bandwidth.



Extended Data Fig. 5. Additional measurement of two-mode squeezing associated with qumode -17 for the trichromatic pump. Electrical spectra showing 2-mode quadrature noise variance (blue) relative to shot noise (gray) for representative qumode pairs. The relative phase between the pump and the LO is scanned over time. All measurements are taken at 0.5 MHz frequency, with 100 kHz resolution bandwidth and 100 Hz video bandwidth.